

## Jerome Rowcroft<sup>1</sup>

Department of Mechanical and  
Aerospace Engineering,  
Monash University,  
Clayton 3800, Victoria, Australia  
e-mail: Jerome.Rowcroft@monash.edu

## David Burton

Department of Mechanical and  
Aerospace Engineering,  
Monash University,  
Clayton 3800, Victoria, Australia  
e-mail: David.Burton@monash.edu

## Hugh. M. Blackburn

Department of Mechanical and  
Aerospace Engineering,  
Monash University,  
Clayton 3800, Victoria, Australia  
e-mail: Hugh.Blackburn@monash.edu

## John Sheridan

Department of Mechanical and  
Aerospace Engineering,  
Monash University,  
Clayton 3800, Victoria, Australia  
e-mail: John.Sheridan@monash.edu

# Siting Wind Turbines Near Cliffs: The Effect of Ruggedness

*Wind farms have often been located in close proximity to coastal cliffs to take advantage of the consistent wind regimes associated with many coastal regions, as well as to extract any available increase in flow speed that might be generated by such cliffs. However, coastal cliffs are often rugged as a result of erosion and the natural shape of the landform. This research explores the impact of the three-dimensional cliff topography on the wind flow. Specifically, wind tunnel testing is conducted, modeling the naturally occurring ruggedness as sawtooth lateral variations of various amplitudes applied to a forward facing step (FFS). Surface shear stress visualization techniques have been employed to derive the flow topology associated with different topographies, while pressure probe measurements are used to measure the development of wind speed and turbulence intensity (TI). Pressure probe measurements and surface pressure taps also assist to determine the lateral and vertical extents of the vortex structures identified. In particular, flow fields characterized by the probe measurements were consistent with vortex bursting that is described by various researchers in the flow over delta wings. Such bursting is observed as a stagnation and corresponding expansion of the vortex. Based on these observations, recommendations are provided for the siting of wind turbines near analogous cliffs. [DOI: 10.1115/1.4041231]*

## Introduction

Steep cliffs and escarpments have long been considered in the context of wind turbine siting, for both their exposed orientation as well as the speed-up that these topographic features induce. The seminal wind tunnel investigation of Bowen and Lindley [1] in 1975 considered wind flow over escarpments of various slopes, including a vertical step, referred to as a forward facing step (FFS). They postulated that the speed-up associated with equivalent topographic features would make them good candidates for siting wind turbines. Since then, many studies have analyzed the flow over the base FFS case—giving particular consideration to the flow structure, describing the regions of flow separation and their change in size as a function of inflow conditions such as the Reynolds number, and the thickness of the boundary layer relative to the height of the FFS and the surface roughness [2–7]. Nevertheless, little work has considered variations to the shape of the FFS. Rowcroft et al. [8,9] considered the effect of wind direction, generating results that might be considered a building block for more complex shapes. Cochard et al. [10] and Montlaur et al. [11], in complementary wind tunnel and computational studies, considered the effect of sawtooth lateral variation of the FFS, also giving consideration to the effect of wind direction. These sawtooth lateral variations mimic rugged coastlines.

In their work investigating the effect of wind direction on flow over FFSs, Rowcroft et al. [9] identified that siting wind turbines 0.5  $h$  downstream of the crest of a FFS of height  $h$ , with the lower tip height maintained above 0.5  $h$ , the rotors would experience the following conditions:

- (1) Consistently high wind speeds across the rotor extent by being above the shear layer.

- (2) Lowest levels of turbulence intensity (TI) by avoiding the recirculation region and its wake.
- (3) Low pitch angles by avoiding the crest region and low veer angles by avoiding the top of the shear layer.
- (4) Avoiding the low frequency buffeting associated with vortices being ejected from the recirculation region.

Cochard et al. [10], giving consideration to the ruggedness of cliffs, completed wind tunnel experiments, where they examined three horizontal planes, the highest of which was at a height of 20.3 mm above their 100 mm sawtooth cliff, and with results presented at a height of 14.3 mm.

In their investigation into siting wind turbines near sawtooth cliffs, Cochard et al. [10] and Montlaur et al. [11] observed delta wing-style vortices forming over the sawtooth protrusions that changed in size as a function of wind direction. They also observed that wind speed varies as a function of height above the surface of the cliffs.

They concluded that siting turbines near such cliffs would have deleterious effects on those turbines because, when the wind direction is not perpendicular to the FFS, the leading delta wing vortex increases in size and strength to cover up to two-thirds of the sawtooth. However, their results did not extend beyond 0.203  $h$  above the surface of the FFS. The development of the delta wing vortices as a function of wind direction is an important finding; however, the question remains as to the vertical extent of those structures, relative to potential wind turbine heights, as this will ultimately determine whether those flow structures will impact wind turbine performance.

The literature related to delta wing vortices is extremely relevant and is useful in understanding the flow behavior over these topographies, particularly in the downstream wake region.

## Brief Review of Delta Wing Vortices and Their Breakdown.

The structure and evolution of a delta wing vortex is the subject of a significant body of academic literature. The flow structure over

<sup>1</sup>Corresponding author.

Contributed by the Fluids Engineering Division of ASME for publication in the JOURNAL OF FLUIDS ENGINEERING. Manuscript received December 3, 2017; final manuscript received August 10, 2018; published online October 4, 2018. Assoc. Editor: Jun Chen.

a delta wing is dominated by two counter-rotating vortices when flow is applied at an angle of attack [12]. These primary vortices induce secondary vortex structures of opposite sign to the primary vortex along the leading edge of the delta wing [12]. Gad-el-Hak and Blackwelder [13] and Lowson et al. [14] identified that the primary vortex structure is itself a merging of smaller vortex pairs. Within this primary vortex structure, various authors observed a Kelvin–Helmholtz instability, before the breakdown of the vortex structure [13,15,16]. According to Gursul’s [16] review of flow over slender delta wings, the shedding frequency associated with this instability was difficult to identify in each case, varying as a function of Reynolds number, as well as being susceptible to external forcing.

The angle of attack plays a role in the topological development of the flow over the delta wing and the breakdown of the delta wing vortex [17]. The angle of attack, which induces an inflow angle over the leading edge of the delta wing, might be compared to the height parameter of the FFS. This suggests that a simple geometric relationship might exist relating the angle of attack of a delta wing and the height of a rugged FFS. However, the insight provided by Pearson et al. [18] suggests that any such relationship is likely to be complex. In their wind tunnel experiments, they used Particle Image Velocimetry to characterize the region upstream of the FFS, and they observed a flow stagnation on the front cliff face at a height of  $0.5h$ , suggesting that the in-flow angle would be largely independent of the height of the cliff.

Downstream of the delta wing apex, Katz [19] identified three modes of vortex development over delta wings, determined by the angle of attack of the delta wing and the sweep angle ( $A/\lambda$ ). The first mode is a symmetric shedding of the primary vortices. At low sweep angles, an increase in the angle of attack results in the delta wing vortices breaking down or bursting. At higher sweep angles, an increase in angle of attack results in the asymmetric shedding of the crest vortices [20,21].

The bursting of the delta wing vortices has been the subject of much research and is ultimately the mechanism that has greatest applicability to the problem of wind turbine siting on sawtooth cliffs. The review by Hall [22] on the breakdown of vortex structures provides a useful description of the vortex breakdown, as well as bringing together various theories on why, when, and how this mechanism occurs.

Hall [22] describes vortex breakdown or bursting as the point where a vortex transitions from having the form of a regular spiral, to having a “very pronounced retardation of the flow along the [vortex] axis and a corresponding divergence of the stream surfaces near the axis [22].” The implication of such a breakdown is that the vortex transitions from being a concentrated, organized, fast-moving stream of fluid to a less concentrated, chaotic region of slow-moving fluid. The unburst vortex remains confined to the near-surface region, allowing the swept area of a rotor to pass

above the structure; the stagnation and consequent expansion of the burst vortex will typically make such a siting technique impossible.

Hall [22] identifies three conditions necessary for vortex breakdown:

- Swirl: Angle of swirl, given by  $\tan^{-1}(v/w)$ , is greater than 40 deg. Azimuthal and axial components of flow velocity are given by  $v$  and  $w$ , respectively.
- Positive pressure gradient along the vortex axis.
- Divergence of stream tubes in the vortex tubes, occurring upstream of the breakdown.

Hall [22] highlights the fact that these conditions are interrelated, and that conditions external to the vortex may induce or retard vortex breakdown. Gursul et al. [23] observed that the transition to vortex breakdown is less abrupt as the sweep angle of the delta wing decreases, or, relating back to the context of the sawtooth FFS, as the  $A/\lambda$  ratio is decreased.

The location of the bursting over the delta wing varies as a function of sweep angle and angle of attack [14]. The location of the vortex bursting has also been shown to vary dynamically, oscillating along the vortex axis, with a characteristic chord-based Strouhal number of the order of 0.03 [16].

**Flow Structure in a Real-World Context.** In highlighting the vertical extent of the vortex structures, it is pertinent to consider the geometry of a utility scale wind turbine in the context of real topography. A classic case of wind turbines sited near rugged coastal cliffs is the Cathedral Rocks Wind Farm (CRWF) in South Australia. It was commissioned in 2007, consisting of 33 Vestas V80 turbines on 60 m towers. The turbines have 80 m rotor diameters. While wind turbine technology might be described as mature, the size of wind turbines has continued to evolve, for example, in 2017, three mainstream wind turbine manufacturers offered onshore wind turbines with rotor diameters of 140 m or more (Vestas V150 (Vestas Wind Systems A/S, Aarhus, Denmark), Enercon E141 (Aurich, Lower Saxony, Germany), Senvion 3.XM140 (Senvion S.A. Hamburg, Germany)). This changes the potential design envelope for the rotor extents from the range of 20 m–150 m to potentially 30 m–200 m or more. In the context of the recommendations of Rowcroft et al. [9], whereby turbines are sited with a lower tip height of half the cliff height, it is not unreasonable for new turbines to have a lower tip height greater than 50 m.

While the CRWF example is only one case, and by no means representative of all cliff-based wind farms, there are many wind farms sited on cliffs and escarpments with heights of approximately 100 m, both in Australia (where this work originates) and in North America and Europe with varying levels of ruggedness, as seen in Table 1. Therefore, understanding the extent,

**Table 1 Nonexhaustive list of operational wind farms potentially affected by flow separation off steep cliffs or escarpments**

Wind farm	Location	Terrain feature height ( $\pm 20$ m)
Woodlawn wind farm	NSW, Australia	110 m
Portland wind farm	VIC, Australia	90 m
Woolnorth wind farm	TAS, Australia	110 m
Cathedral rocks wind farm	SA, Australia	140 m
Starfish hill wind farm	SA, Australia	150 m
Albany wind farm	WA, Australia	70 m
Nine mile beach wind farm	WA, Australia	70 m
Hawi wind farm	Hawi, HI	50 m
Pakini nui wind farm	Naalehu, HI	170 m
Neshgashi	Eysturoy, Faroe Islands	120 m
Fécamp	Normandy, France	110 m
Wind point wind farm	Washington, DC	400 m
Madeira—Various	Madeira, Portugal	100 m–1500 m
Rhodes wind farm	Rhodes, Greece	150 m
Project west wind	Wellington, New Zealand	150 m

Note: Cliff heights are estimated from Google Earth.

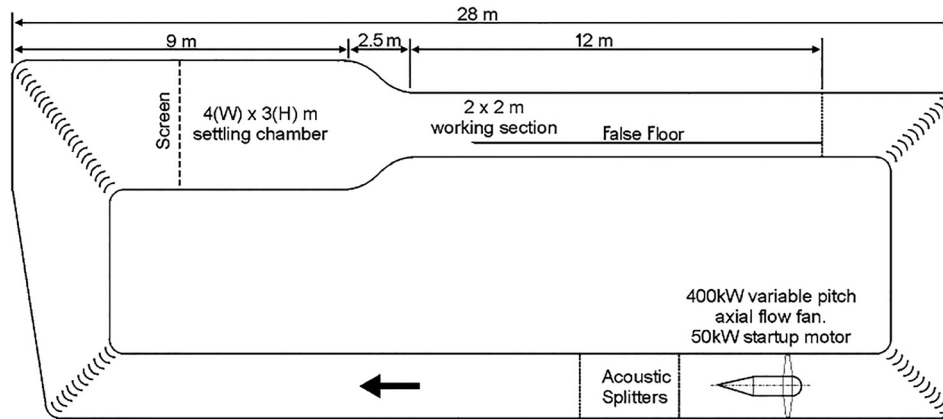


Fig. 1 Schematic of Monash University 450 kW wind tunnel

persistence, and location of the vortex structures is critical information to the wind energy engineers in appropriately siting turbines in the vicinity of cliffs, as well as understanding the loads experienced by the existing wind turbines.

From the discussion previously, there are a number of key questions that are worthy of further investigation. In this paper, the two following questions are examined. First, does the extent of the vortex evolve with the amplitude of the sawtooth protrusion? And second, what is the vertical extent of the delta wing vortices?

To this end, we present a series of wind tunnel experiments. First, the effect of varying the amplitude of the sawtooth protrusion is investigated by mapping the flow topology for a number of sawtooth amplitudes using paint droplet visualizations, similar to those performed by Rowcroft et al. [8], and surface pressure measurements.

Second, based on that initial topological mapping, two selected cases are examined in greater detail using four-hole pressure probes (Cobra Probes) to map the velocity field. This provides valuable insight into the vertical extent of the vortex cores as they propagate from the tip of the sawtooth into the far wake, as well as providing a mapping of the velocity field.

While aiming to generate scalable and broadly applicable results, there are some notable limitations. The work of Goruney and Rockwell [24] on flow over delta wings with sinusoidal leading edges highlights that even minor deviations from the “ideal” shape have significant impacts on flow topology; similarly, the work of Lange et al. [25] illustrates the impact on wind turbine yield of incorrectly modeling the crest of a cliff, with the vertical extent of vortex structures reduced when the sharp leading edge is rounded. Similarly, atmospheric stability and boundary layer shape and thickness will each impact on the flow field, and ultimately on the performance of a wind energy facility embedded in that flow field [26]. The comparison by Rowcroft [27] of his FFS data with the scanning LIDAR data collected at Bolund Hill by Mann et al. [28] highlights that while the flow features are comparable, the precise magnitude and shape is highly site specific.

## Methodology

Wind tunnel testing was performed over a range of models. Three wind tunnel techniques were implemented: surface shear stress visualization; Cobra Probe measurement; and surface pressure measurement.

**Wind Tunnel and Models.** The research was conducted in the Monash University 450 kW wind tunnel, as shown in the schematic in Fig. 1. The wind tunnel is fan blade pitch controlled. The working section of the tunnel has a 2 m × 2 m cross section and extends 12 m. Testing was completed in the center region of the

working section over a false floor. Further details of the wind tunnel and the inflow conditions are specified in Rowcroft et al. [9].

Experiments were performed at a fan blade pitch angle of 30 deg, corresponding to a freestream speed of  $34 \text{ ms}^{-1}$ , over FFSs of height,  $h = 0.050 \text{ m}$ . The experiments were completed at Reynolds Numbers of  $1 \times 10^5$ , using the step height,  $h$ , as the reference length and freestream velocity as the reference velocity. End plates extended  $12h$  upstream of the models. The models resulted in 2.5% blockage and extended beyond  $10h$  downstream, and can be thus considered isolated cliffs according to Moss and Baker [5]. The aspect ratio was 34, allowing four complete periods of the geometry to be modeled. The lateral variation of the FFSs explicitly segments the flow, minimizing any impacts associated with aspect ratio. The experimental layout is shown in Fig. 2. The models were painted with semigloss enamel paint and were aerodynamically smooth. The geometric parameters are presented in Table 2.

**Inflow Conditions.** Vertical profiles of velocity, TI, and stream-wise integral length scale profiles are presented in Fig. 3. Conditions were developed over a false floor, with a fetch of  $32h$ . No additional roughness was applied to the fetch. The inflow conditions were measured by traversing with a Cobra Probe at a frequency of 5000 Hz and down-sampled to 2500 Hz for 180 s. The freestream TI was 1% and the boundary layer thickness,  $\delta$ , was 100 mm. The integral length scale was calculated by fitting the von Kármán equation to the power spectral density. The resulting boundary layer thickness to step height ratio,  $\delta/h$ , was 2. The shear exponent,  $\alpha$ , derived from the gradient of the natural logarithm of velocity plotted against the natural logarithm of height through the boundary layer, as shown in the left panel of Fig. 3, was 0.0907. The inflow configuration is described in Rowcroft et al. [9], where detailed descriptions of the instrumentation, configuration, and the inflow conditions were provided. An upstream Pitot-Static tube was used to normalize the Cobra Probe measurements. The Pitot-Static tube was located greater than  $55h$  upstream of the model location, 12.3 boundary layer heights above the surface of the false floor.

The motivation of this work is to characterize the underlying flow structures that develop over cliffs, hence, it was desirable to minimize TI levels. Cliff-top wind farms often have ocean fetches. Atmospheric boundary layers developed over ocean fetches tend to be thinner, particularly under stable and near stable conditions, with various sources modeling gradient heights in the order of 200 m [29,30]. Stable and near stable conditions also act to suppress turbulence. Thus, the  $\delta/h$  ratio of 2 used in this experimental setup might be considered representative of a 100 m high coastal cliff, although the freestream TI of 1% is still low compared to typical values of 5–10% for offshore applications [31].

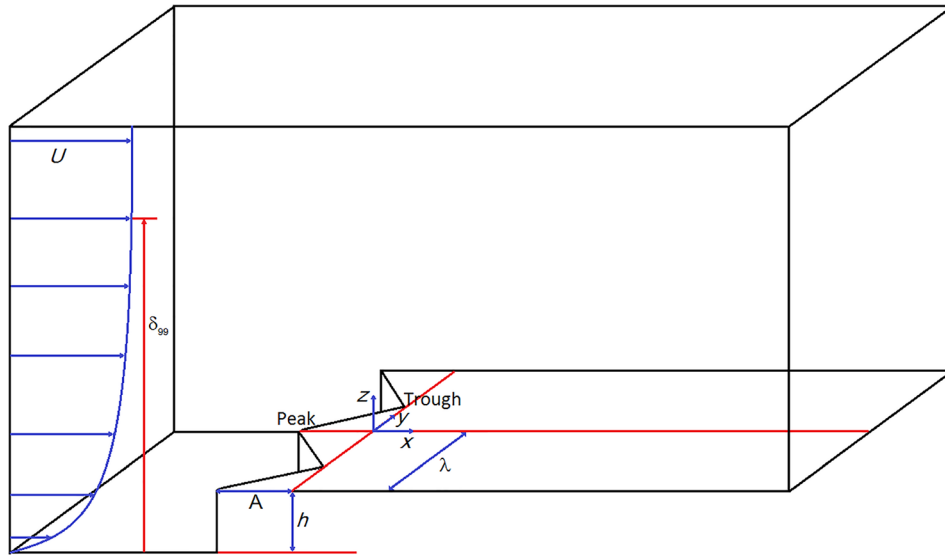


Fig. 2 Experimental domain

Table 2 Geometric parameters

Height ( $h$ )	$A/\lambda$	Amplitude ( $A$ )	Wavelength ( $\lambda$ )	Sawtooth half angle	Extent downstream	Aspect ratio (width/height)
0.050 m	0.325	0.130 m	0.400 m	33 deg	2.6 m (52 $h$ )	34
0.050 m	0.5	0.200 m	0.400 m	45 deg	2.6 m (52 $h$ )	34
0.050 m	0.65	0.260 m	0.400 m	52 deg	2.6 m (52 $h$ )	34
0.050 m	1	0.400 m	0.400 m	63 deg	2.6 m (52 $h$ )	34

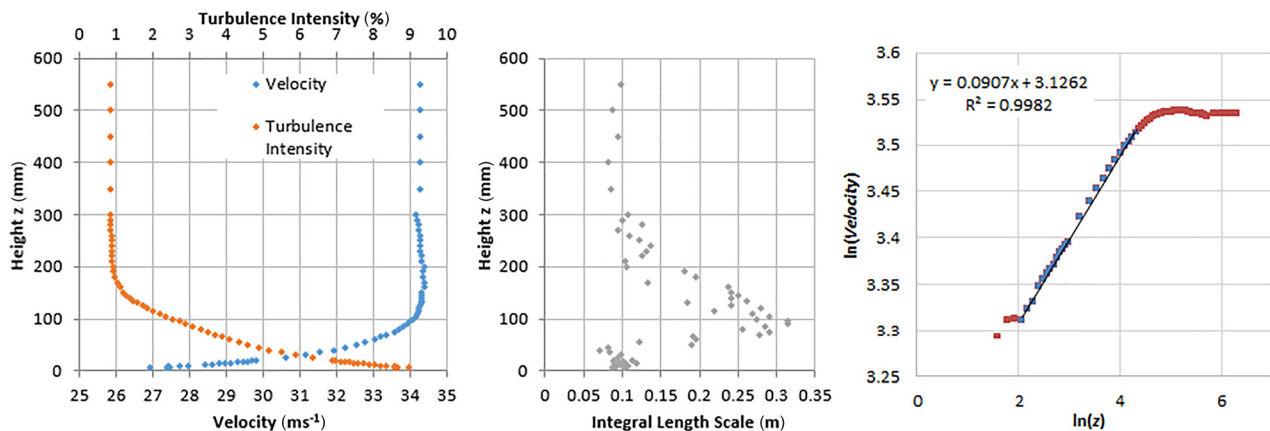


Fig. 3 Inflow conditions: Panel 1—velocity and stream-wise TI; Panel 2—stream-wise integral length scale, and Panel 3—natural log of height plotted against natural log of velocity, with the gradient giving the power law exponent,  $\alpha$

**Surface Shear Stress Visualization.** A paint droplet visualization technique was implemented to depict the surface shear stress, showing the direction at which the surface shear stress acts and giving an indication as to the magnitude of the surface shear stress.

In each case, the surface of the model was aerodynamically smooth, covered with black, semigloss enamel paint. This provided a consistent surface, allowing the paint to streak easily over the surface. Magenta-colored water-based paint was diluted with tap water to approximately a 1:1 ratio to provide a paint mix with sufficient viscosity to avoid speckling, but not so viscous as to stop the droplets from streaking.

Nominally 0.1 mL of the paint solution was applied at a number of points using hypodermic syringes. To obtain the streaks, the wind tunnel was run up to a fan blade pitch angle of 30 deg,

corresponding to a freestream velocity of  $34 \text{ ms}^{-1}$ . The paint could typically be observed to begin streaking at a fan blade pitch of 25 deg. The wind tunnel was allowed to run at speed for approximately one minute from the time the wind tunnel fan blade pitch reached 30 deg. This allowed the streaks sufficient time to form. This process was repeated, with more droplets added until a sufficiently high resolution was obtained. An example is shown in Fig. 4.

From these surface shear stress visualization techniques, it was possible to deduce the mean flow topology over the surface of the models. Perry and Chong [32] provide means of interpreting the streaks in terms of flow structures, identifying separation and reattachment lines, stable and unstable nodes and foci, and saddle points.

**Cobra Probe Measurements.** Turbulent flow instrumentation (TFI) Cobra Probes have been used to collect dynamic velocity

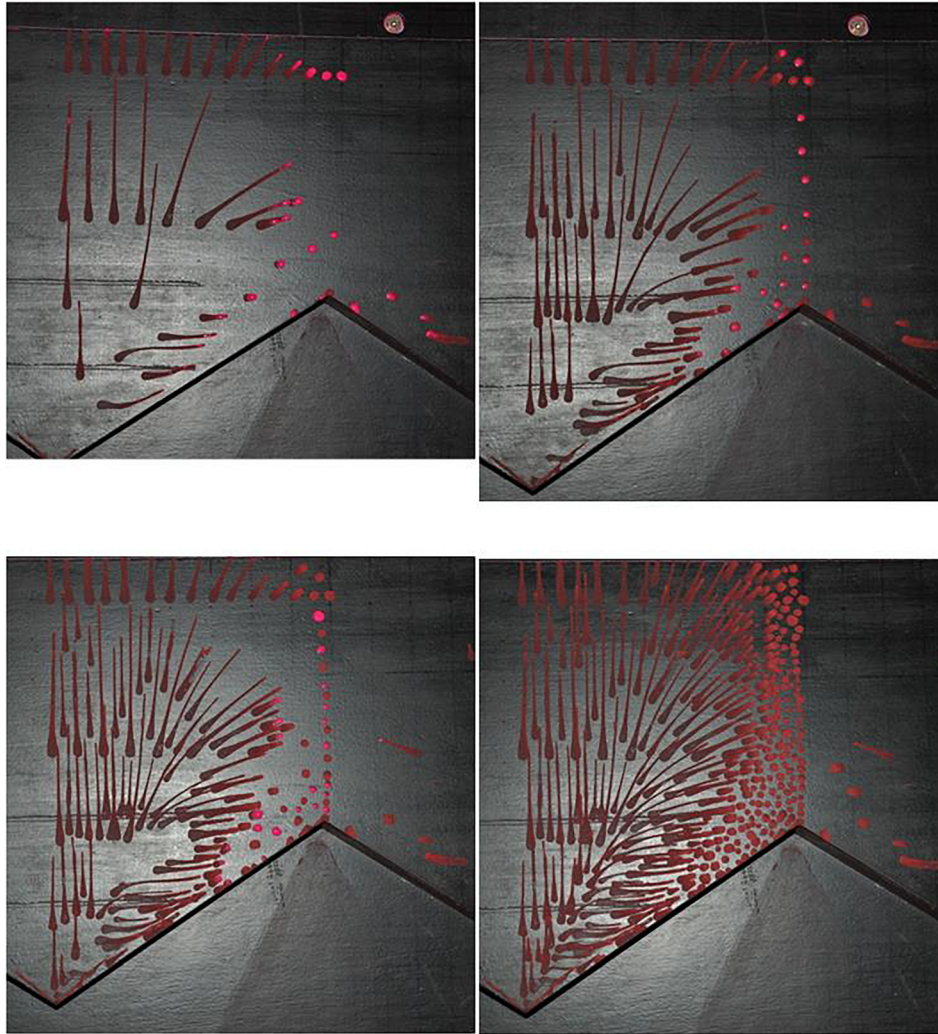


**Fig. 4 Demonstration of build-up technique. Four instances are shown. Intermediate steps are omitted for brevity. Flow is from bottom of page to top.**

data, as well as mean statistics above the surface. The Cobra Probe acts as four Pitot-static tubes arranged to capture flow from within a 45 deg cone of acceptance. The development and the performance of Cobra Probes are described by Hooper and Musgrove [33,34] and Musgrove and Hooper [35]. These probes have been used extensively in the characterization of bluff body wakes [36,37].

The input data were logged using the TFI Device Control software. Sample lengths were 180 s, at a sampling frequency of 2500 Hz, down-sampled from 5000 Hz. Cobra Probes were used to measure the inflow conditions, as well as traversing over the  $A/\lambda = 0.325$  model and regions of the  $A/\lambda = 0.5$  model.

Various investigations have been conducted to establish the accuracy of the Cobra Probes, considering both their static response and their dynamic response. Hooper and Musgrove [33] showed that they are insensitive to Reynolds number for the velocity range  $16 \text{ ms}^{-1}$ – $110 \text{ ms}^{-1}$ , giving confidence in the mean data over a broad velocity range, below speeds where measurements would be sensitive to compressibility. Hooper and Musgrove provided further dynamic validation of the Cobra Probe performance in a swirling jet [35], and validated their results against hot wire anemometers and laser Doppler anemometers in fully developed pipe flow [34]. These results demonstrated excellent frequency response up to 1500 Hz. Additionally, Chen et al. [38], in developing the calibration methodology of the Cobra Probes, suggested that the errors in the calibration surfaces

affecting the pitch and yaw angles measured by the probes would be 2 deg, in addition to a 0.5 deg uncertainty associated with the alignment of the Cobra Probe relative to the stream-wise axis. They also reported an uncertainty in velocity of 2% associated with the calibration surface and an additional 0.5% uncertainty in velocity due to the calibration procedure caused by an increase in static pressure near the potential core of nozzle jets, typically used to calibrate Cobra Probes [38].

This uncertainty propagates through derived quantities, for example, the speed-up ratio,  $S$ , which is the ratio of the normalized Cobra Probe measurement over the geometry to the corresponding normalized Cobra Probe measurement through the undisturbed boundary layer, with the Cobra Probe measurements normalized against the upstream Pitot-Static tube. The 2% uncertainty associated with the calibration surface is considered as a bias error, while the additional 0.5% is treated as a random error. Similarly, the uncertainty associated with the Pitot-Static tube is assumed to be a random error of 1.5%. In this context, the Cobra Probe uncertainties can be combined using a root-sum-square approach. Combining the errors in this way for typical velocity and speed-up values ( $U = 30 \text{ ms}^{-1}$ ,  $S = 1.07$ ) gives an uncertainty of 4%.

In contrast, the turbulence intensity ratio (TI ratio), which is the ratio of the turbulence intensity over the geometry to the corresponding turbulence intensity in the undisturbed boundary layer, is affected by only the random uncertainty, as the calculation of

the standard deviation relies on the difference between the mean and the instantaneous velocity, which cancels the bias error, while the random uncertainty propagates through the difference, sum, square, and square root elements of the standard deviation calculation, as well as through the quotient of the standard deviation and the velocity, and between the two turbulence intensity values. For a representative TI ratio of 3, this error propagation yields an uncertainty of approximately 7% giving a TI ratio of  $3.0 \pm 0.2$ .

**Surface Pressure Measurement.** Surface pressure taps were used to capture transient surface pressure data over the surfaces of the sawtooth models. Between 120 and 125 pressure taps were used on each model, allowing quantification of peak and mean pressures and instantaneous pressure distribution.

Turbulent flow instrumentation dynamic pressure measurement system (DPMS) was used, providing 128 input channels, across two DPMS units, with a maximum measurement range of  $\pm 7$  kPa. The input data were logged using the TFI Device Control software. 180 s samples were collected at a sampling frequency of 1000 Hz.

Each pressure tap was linked to the manifold connected to the DPMS unit with a 1 m PVC tube with inner diameter of 1.2 mm. The tubes were purged with nitrogen.

Results are presented as pressure coefficients,  $C_p$ , according to the following equation:

$$C_p = \frac{P - P_\infty}{Q_\infty} \quad (1)$$

In the equation,  $P$  is the local pressure, measured at the surface,  $P_\infty$  is the reference pressure, measured at the surface, upstream of the FFS, and  $Q_\infty$  is the dynamic pressure of the freestream flow.

A root-sum-square analysis of the uncertainty, considering the manufacturer's specification of the DPMS units (0.1% of full-scale) and the uncertainty of the freestream dynamic pressure, suggests an uncertainty of 4% for typical values of the pressure coefficients.

## Results and Discussion

In this section, the flow topology associated with each geometric variation is derived from the surface shear stress visualizations and discussed. Surface pressure measurements for each case provide further insight into the development of the flow as  $A/\lambda$  is varied. Detailed analysis including Cobra Probe measurements of the shallowest cases ( $A/\lambda = 0.325, 0.5$ ) is presented.

**Surface Shear Stress Visualizations and Flow Topology.** The surface shear stress flow visualizations, for all amplitude ratios tested, are shown in Fig. 5. These capture the mean surface shear stress fields. From the surface shear stress visualizations, surface flow topology can be determined, identifying critical lines and points and ultimately quantifying the interaction between the vortex structures that are generated over the topography. The distribution of critical points is determined by the Poincaré–Bendixson theorem that  $\sum N - \sum S = (\epsilon/2\pi)$ , where  $N$  denotes the number of node points on the plane and  $S$  denotes the number of saddle points on the plane and  $\epsilon$  denotes the angle through which the shear stress vector passes over the plane (here, the upper surface of the cliff) [39]. Over this FFS geometry  $\epsilon = 0$  deg, thus, the number of node points must equal the number of saddle points. A labeled schematic of the flow topology is presented in Fig. 6 and each of the derived flow topologies is presented in Fig. 7.

The surface shear stress visualizations in Fig. 5 are, in all cases, consistent with the existence of a longitudinal rotating structure with a primary attachment line near, but not exactly, aligned with the crest of the sawtooth. This is similar to that seen by Hoerner and Borst [12] and Werle [40] who identified the formation and decay of vortices over delta wings and Cochard et al. [10] who identified the formation of these vortex structures over FFSs with sawtooth lateral variation and drew the parallel to rugged cliff topography.

The angle between the primary attachment line and the crest is referred to as the Vortex Growth Angle, and is illustrated in Fig. 6. It can be associated with the scale of the vortex and remains constant for a period along the crest. This implies linear vortex growth. The primary attachment line then turns downstream, with a positive bifurcation line evident in each of the cases. It is clear that the peak of the sawtooth is associated with genesis of this structure, as the primary attachment line can be traced to the peak of the sawtooth. The orientation of the primary attachment line relative to the crest is plotted against the orientation of the crest relative to the freestream flow in Fig. 8. The orientation of the crest relative to the freestream flow is referred to as the Sawtooth Half Angle and is also illustrated in Fig. 6. Figure 8 highlights the linear growth of the vortex. In Fig. 8, a theoretical point has been added: at the Sawtooth half angle of 90 deg, which would result in a vortex growth rate of 0 deg. The gradient and the intercept of this plot imply that at a Sawtooth Half Angle of 0 deg, which is the base FFS case, the reattachment line will extend at a 45 deg angle from the edge of the crest, at its interface with the end plate. However, for the cases examined here, the footprint of the vortex on the surface of the sawtooth protrusion accounted for between 43% and 53% of the area.

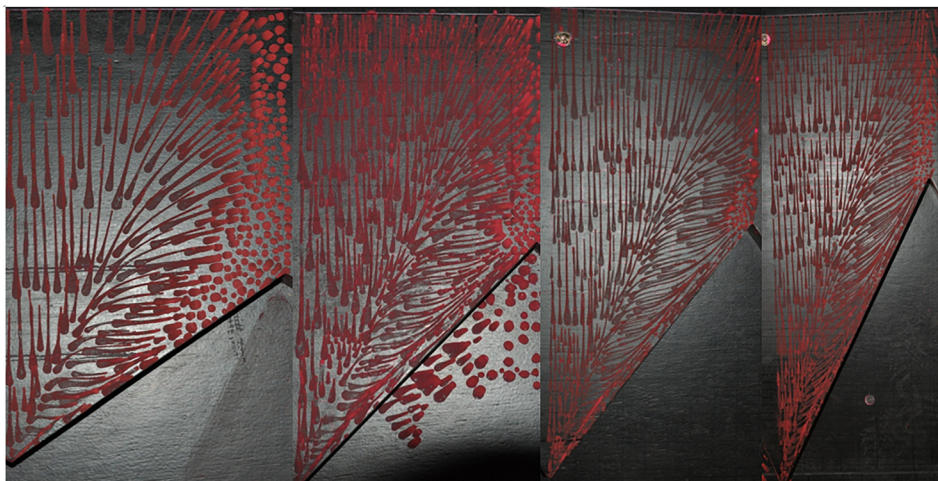


Fig. 5 Surface shear stress visualizations for the four  $A/\lambda$  ratios used, from left to right  $A/\lambda = 0.325, 0.5, 0.625, \text{ and } 1$

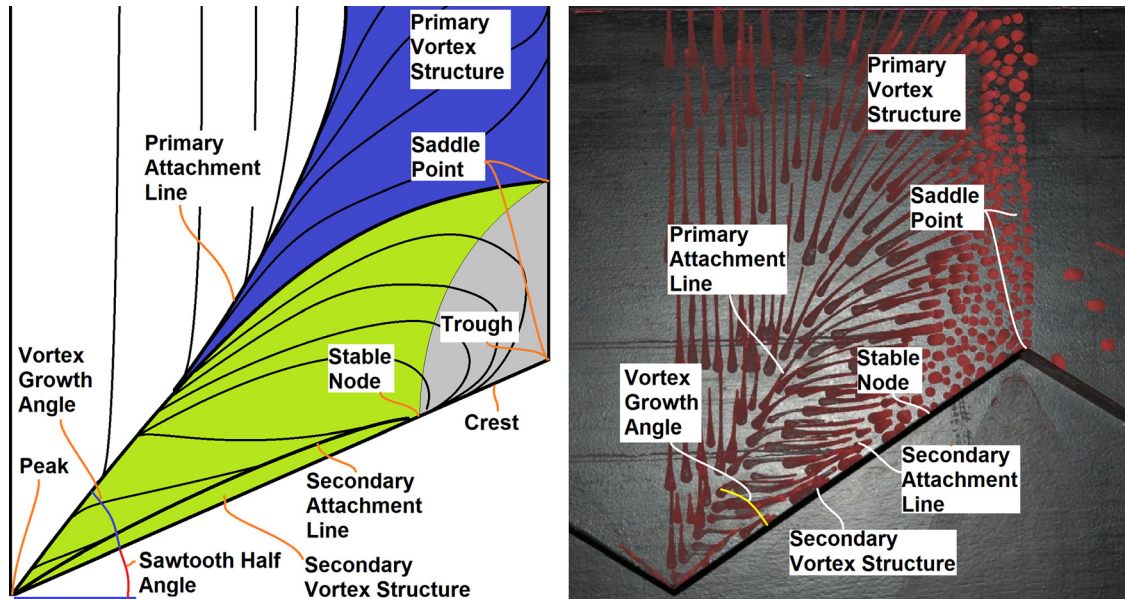


Fig. 6 Schematic of flow topology compared with photograph of streaks, with descriptions of topological and geometric parameters

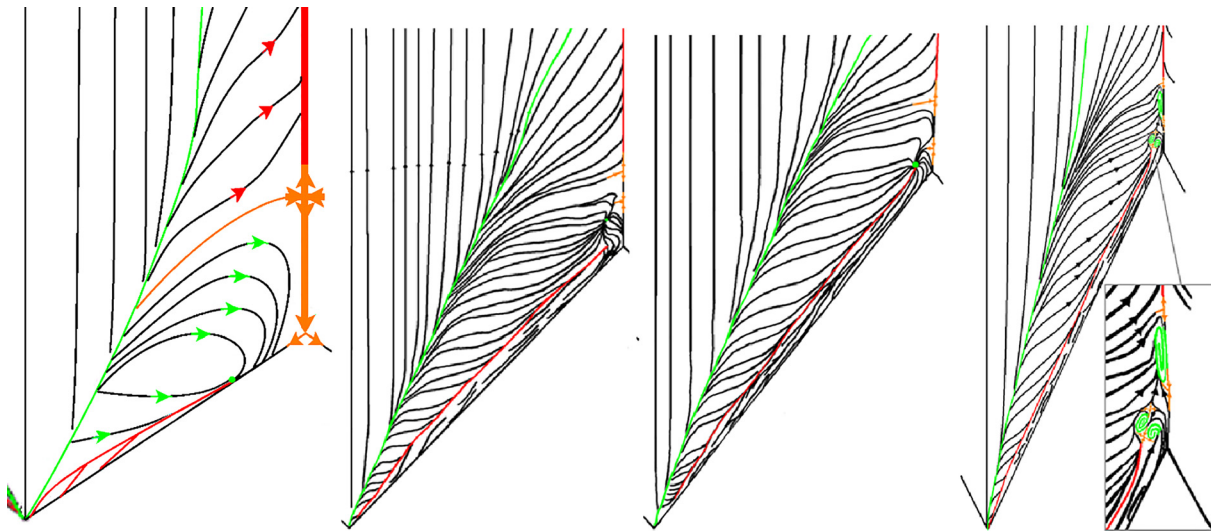


Fig. 7 Flow topology over a FFS with sawtooth leading edge. From left to right,  $A/\lambda = 0.325, 0.5, 0.65,$  and  $1$ . Flow is from bottom of page to top. Saddle points can be identified based on direction arrows. Stable nodes and foci – points of convergence are indicated by lighter colored dots and spirals. A close-up of the trough region for the  $A/\lambda = 1$  case is shown in the inset.

As  $A/\lambda$  increases, the primary vortex remains attached over a larger portion of the crest. In each case, both the primary vortex and the secondary vortices channel flow along the crest. The visualizations were not of sufficient resolution to fully characterize the secondary vortices that occur between the primary vortex and the crest, but we expect that there is not merely a single secondary vortex that is induced, but rather an ever increasing number of secondary vortices, all acting in a counter-rotating fashion to their neighbor [41], each having a strong component near parallel to the sawtooth.

In the three shallower cases, the stable node is where the primary vortex, the secondary vortex, and the recirculating flow that occurs between the two saddle points all converge, as can be seen in Fig. 7.

The saddle points represent the convergence of dividing shear stress lines. The lines that they form delineate the flow structures.

The downstream saddle point is more straightforward to characterize—it is the intersection between the line of symmetry that runs in the streamwise direction, and what would be described as the separation line downstream of a straight-edged FFS. Upstream of this line, flow is entrained back toward the stable node. Downstream of this line, flow is entrained downstream. Of course, the flow that is entrained downstream forms part of the single coherent primary vortex resulting in much higher magnitudes of shear stress in this region, and by extension the flow speed, when compared to the region of flow recirculating back toward the stable node. This is observable in the surface shear stress visualizations presented in Fig. 5.

The second saddle point is again on the line of geometric symmetry. But it forms the delineation between the recirculating flow described in the previous paragraph, and the freestream flow when the stable node is on the crest, or the secondary vortex structure.

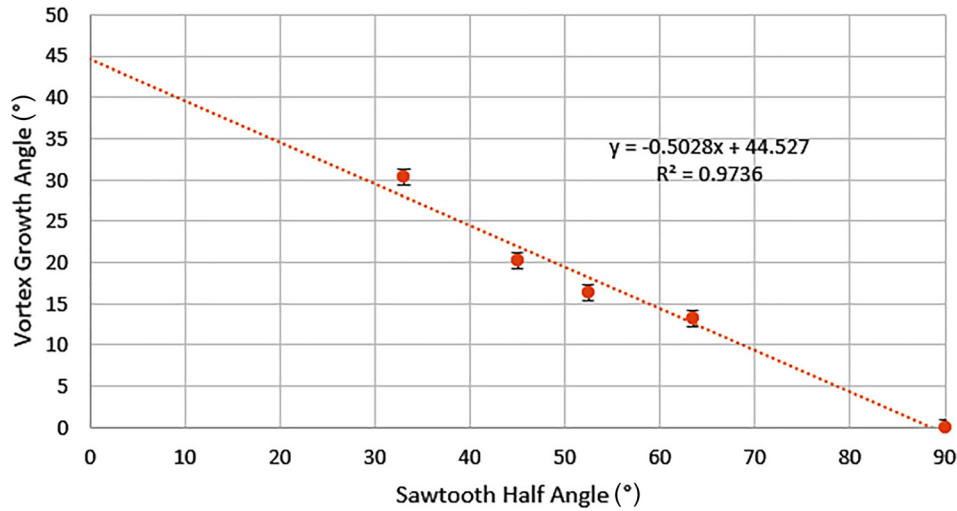


**Fig. 8 Vortex growth angle as a function of Sawtooth half angle. Vortex growth angle is measured at the sawtooth peak, between the crest and the primary attachment line.**

Interpolating between the  $A/\lambda = 0.325$  and  $A/\lambda = 0.5$  cases, it can be surmised that the stable node would progress downstream along the crest with increments of  $A/\lambda$ . By  $A/\lambda = 0.5$ , the secondary vortex structure has already increased in size, strength, and stream-wise momentum such that the stable node is pushed onto the surface proper—the result of a kind of “overshoot” from the secondary structure, which then requires the flow to feed back into the stable node. In the  $A/\lambda = 0.65$  case, the same basic structure is in place, however, there appears to be greater swirl, as the secondary structures funnel back to the stable node. From a topological perspective, actual change in the structure of the flow is observed only between the  $A/\lambda = 0.65$  and  $A/\lambda = 1$  cases. The increment to  $A/\lambda$  drives an increase in swirl around the stable node, which, we hypothesize, forms a stable focus. The stable focus driven by the secondary structures causes its vortex pair to roll up between itself and the streamwise motion of the primary vortex.

A key development observed through the increments of  $A/\lambda$  is that lower values of  $A/\lambda$  result in a larger vortex footprint on the surface of the FFS. This is consistent with the observations of Cochard et al. [10] and Montlaur et al. [11] and their work on varying the wind direction over the cliffs. Cochard et al. [10] noted, for their symmetric  $A/\lambda = 0.5$  case, that when the wind speed was perpendicular to the FFS, the vortex footprint of each delta wing vortex occupied approximately one-third of the top surface of the sawtooth element; as they applied a yaw angle, the upwind vortex occupied a greater proportion of the top surface, while the downwind vortex occupied a smaller proportion. The change in  $A/\lambda$  can be equated with a change in the wind direction for the flow directly above the protruding sawtooth element. Beyond the trough, where the two delta wing vortices interact, the equivalence cannot hold as the strength of each vortex is imbalanced. Montlaur et al. [11] demonstrate in their computational fluid dynamics simulations the persistence into the far wake of the pair of counter-rotating vortices, in spite of their imbalance.

While detailed topological characterization is interesting from a fluid mechanics perspective, it is necessary to infer what is happening above the surface so as to draw conclusions pertaining to wind turbine siting. From the surface patterns alone, it is clear that not only is there a significant stagnation around the sawtooth trough locations, but that in shallower cases (lower values of  $A/\lambda$ ), this stagnation occurs farther upstream, and in deeper cases (higher values of  $A/\lambda$ ), the stagnation occurs farther downstream. Additionally, the stable nodes necessitate a strong up-draft, which, again, occur in the vicinity of the troughs. Rowcroft et al. [9] showed that a developed recirculation region downstream of a yawed FFS is associated with notable increases in turbulence intensity in regions between the crest and the length of the mean recirculation bubble

beyond one cliff height. Their measurements also highlighted the vertical extent of the increased TI into the far wake.

In Cobra Probe Measurements section of this paper, a mapping of point measurements using Cobra Probes is presented over the shallowest of the models—the  $A/\lambda = 0.325$  case, as well as point-based measurements downstream of the trough region in the  $A/\lambda = 0.5$  case.

**Surface Pressure Measurements.** Mean surface pressure coefficients from different cases are presented in Fig. 9, with the derived flow topology superimposed. These plots demonstrate consistency with the extent of the vortex structures observed in the surface shear stress visualizations, and illustrate the location and magnitude of the highest mean negative pressures as a function of the amplitude of the sawtooth.

In each of the cases, the primary attachment line is aligned with a region of high negative pressure, while the pressure coefficients along the attachment line approach zero. The vortex structures result in large negative pressures, however, at the attachment line, the flow impinges on the surface resulting in a high-pressure region. This is most clearly observed for the  $A/\lambda = 0.5$  case, as this case had the highest concentration of pressure taps in this region.

**Cobra Probe Measurements.** The structure of the flow over the variously shaped sawtooth FFSs has been detailed in the Surface Shear Stress Visualizations and Flow Topology section. In this section, results from Cobra Probe measurements are used to measure the flow over the  $A/\lambda = 0.325$  case and downstream of the trough region in the  $A/\lambda = 0.5$  case. For the  $A/\lambda = 0.325$  case, contour plots of speed-up and TI ratio are presented in Figs. 10 and 11, respectively. Using the trough point as a reference, the measurement planes are located at the peak ( $x/h = -2.6$ ), halfway along the sawtooth protrusion ( $x/h = -1.3$ ), at the trough ( $x/h = 0$ ), downstream of the trough ( $x/h = 2$ ), and in the far wake ( $x/h = 10$ ).

The speed-up is given by the following equation:

$$S = \frac{\frac{U(x, y, z)}{U_P}}{\frac{U_{BL}(x = 0, y = 0, z)}{U_{P,BL}}} \quad (2)$$

$U(x, y, z)$  is the magnitude of the velocity vector at a point  $(x, y, z)$ , according to the Cartesian coordinate system defined in Fig. 2.  $U_P$  is the magnitude of the velocity vector measured at the

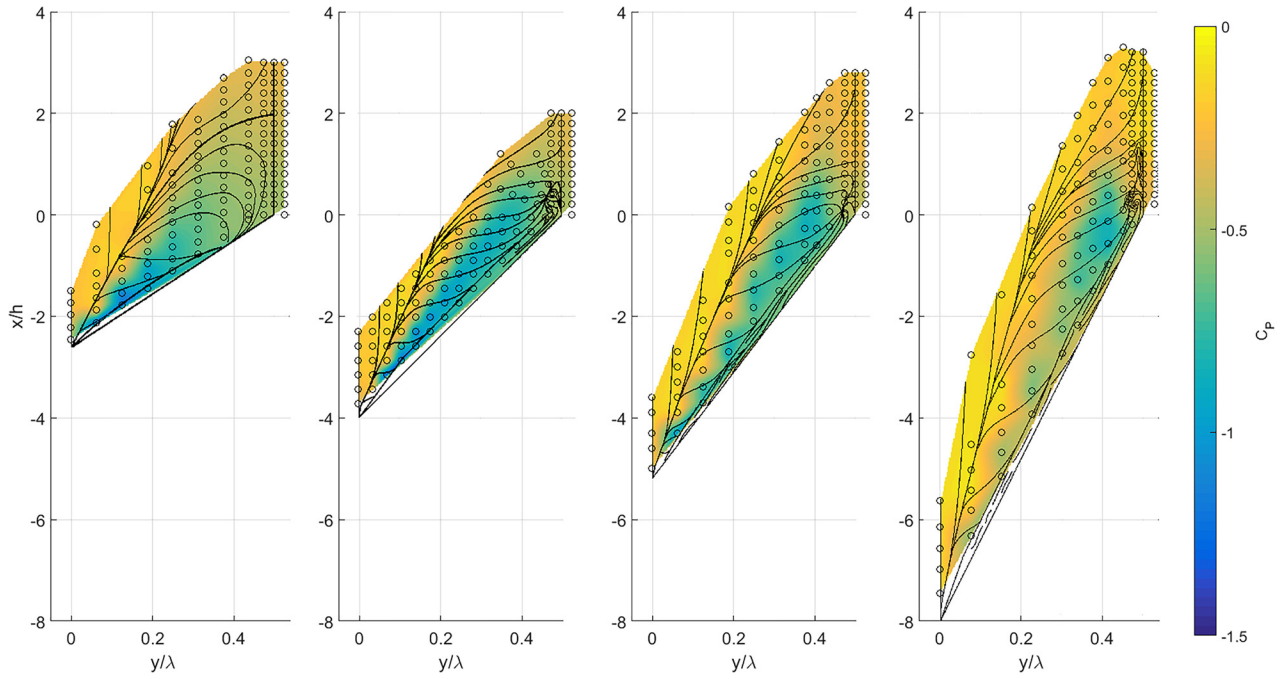


Fig. 9 Surface pressure coefficients overlaid with flow topology; measurement locations denoted by circles

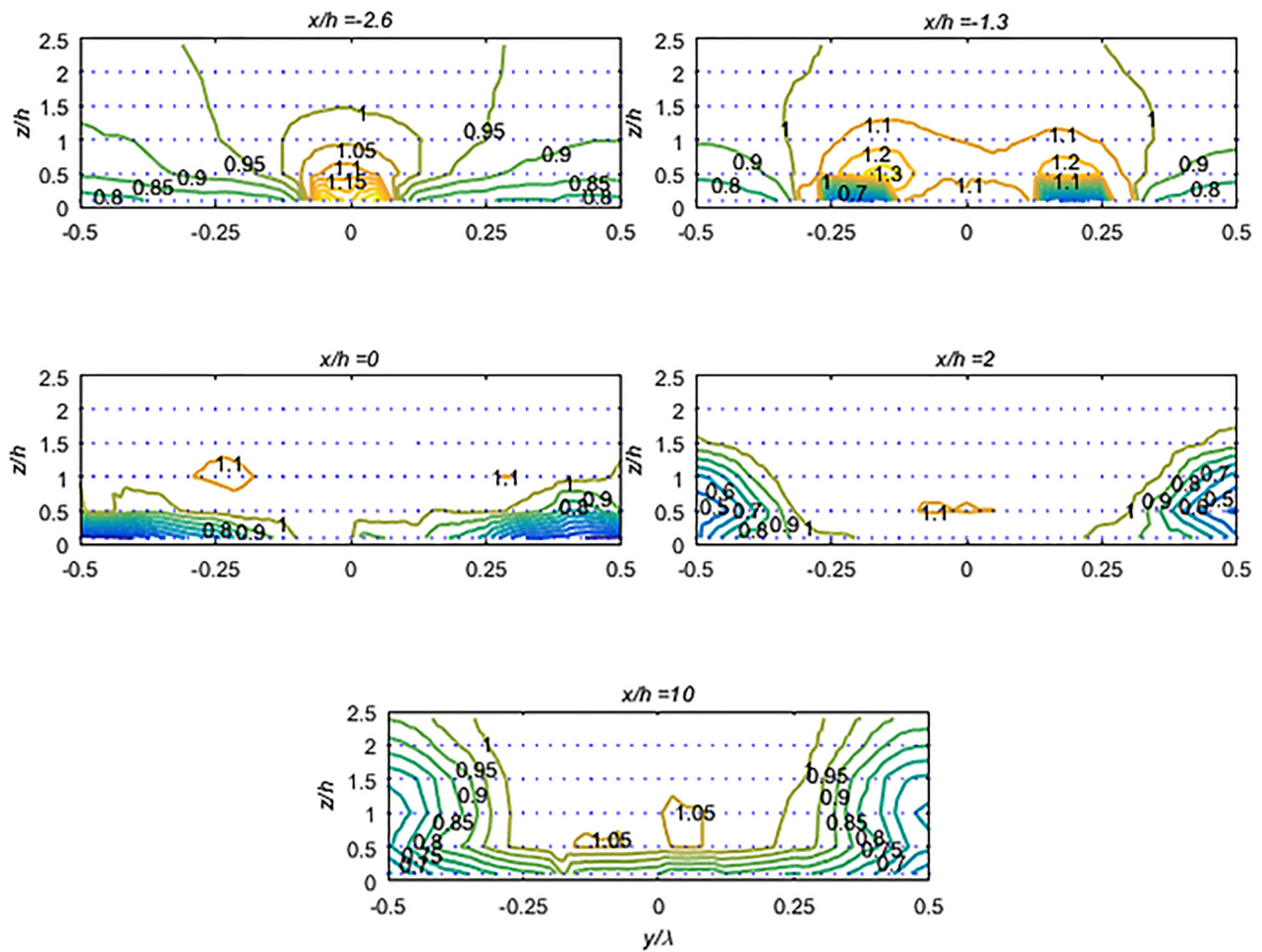


Fig. 10 Speed-up contours above the  $A/\lambda = 0.325$  topography

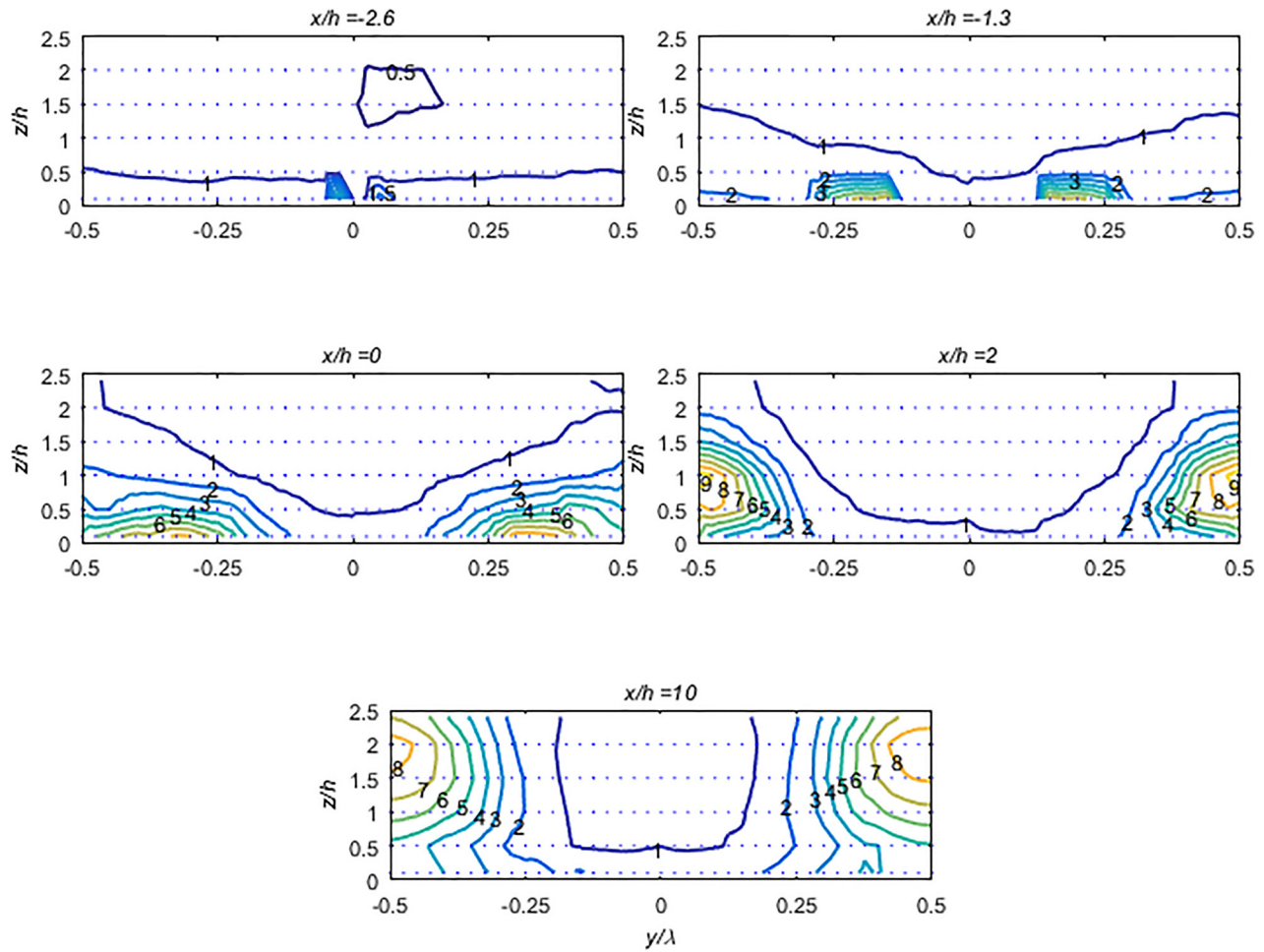


Fig. 11 Turbulence intensity ratio contours above the  $A/\lambda = 0.325$  topography

upstream Pitot-Static tube, measured concurrently to  $U(x, y, z)$ .  $U_{BL}(x=0, y=0, z)$  is the magnitude of the velocity vector in the undisturbed boundary layer, that is, without the model in place, at  $x=0, y=0$ .  $U_{P,BL}$  is the magnitude of the velocity vector measured at the upstream Pitot-Static tube, measured concurrently to  $U_{BL}(x=0, y=0, z)$ .

Similarly, the TI ratio is given by

$$\text{TI ratio} = \frac{I_{uvw}(x, y, z)}{I_{uvw,BL}(x=0, y=0, z)} \quad (3)$$

$I_{uvw}(x, y, z)$  is the TI based on the three velocity components and is defined here

$$I_{uvw} = \frac{\sqrt{\frac{1}{3}(\overline{u^2} + \overline{v^2} + \overline{w^2})}}{U} \quad (4)$$

The BL subscript and the  $(x, y, z)$  location have the same meaning as in the equation for speed-up.

The vortex structure is evident as sets of annular contours in both the speed-up plots in Fig. 10 and the TI ratio plots in Fig. 11, which is consistent with the work of Cocharde et al. [10] and Monlaur et al. [11]. Above the sawtooth element ( $x/h = -2.6, -1.3$ ), the speed-up contours are dominated by regions greater than unity, while the plane aligned with the trough ( $x/h \geq 0$ ), the speed-up contours are dominated by values less than unity—that is, a slow-down relative to the undisturbed inflow conditions, which is evident through the vortex structure as it propagates

downstream. The TI ratio contours appear more sensitive to the vortex structures. At  $x/h = 0$ , where the speed-up contours are spread further laterally than they are vertically, the TI ratio contours are observed to have extended vertically to a greater extent, impacting regions above  $z/h = 1$ .

*Experimental Observations in the Context of the Delta Wing Literature.* In this section, the point-based measurements are analyzed together with the surface pressure measurements. This analysis demonstrates that the vortices observed do undergo this same bursting behavior, impacting the vortex footprint, and the vertical extent of the vortex. The resulting extents of the vortex structures directly impact on the suitability of a location for siting a wind turbine.

Examining the first pane of Fig. 9, the surface pressure is presented for the  $A/\lambda = 0.325$  case. There is a clear positive pressure gradient along the core of the primary vortex setting up conditions for vortex bursting, according to Hall's second criterion [22].

The velocity profiles in Fig. 10 provide further contrast between the compact stream of fast moving flow and the “very pronounced retardation of the flow along the [vortex] axis and a corresponding divergence of the stream surfaces near the axis [22]”. At the topographic apex, ( $x/h = -2.6$ ), the speed-up is dominated by values greater than unity (an increase in speed relative to inflow conditions), which is consistent with the description, above. At  $x/h = -1.3$ , that is, halfway along the sawtooth protrusion, the speed-up is delicately balanced between the fast-moving flow and the flow stagnation, with speed-up as low as 0.7 measured at the base of the vortex structure, and exceeding 1.3 at the top of the

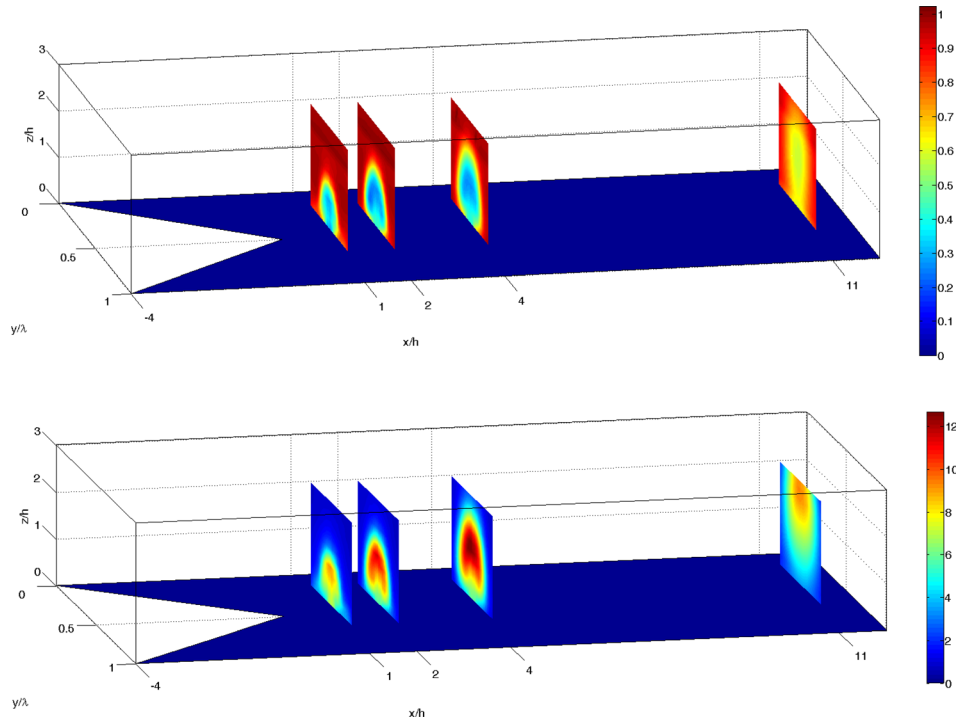


Fig. 12 Speed-up (top) and TI ratio (bottom) measurements over the  $A/\lambda = 0.5$  case

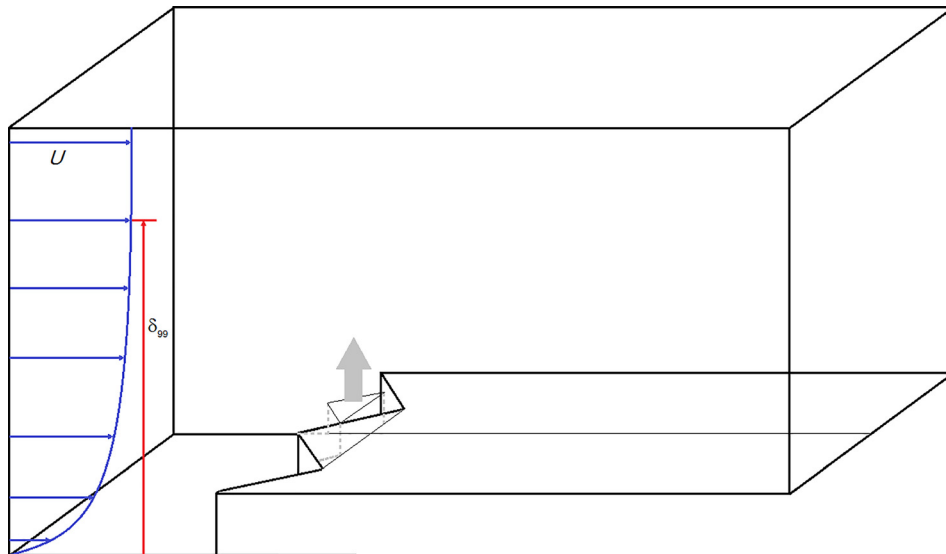


Fig. 13 Siting approach over rugged cliffs. Gray dashed lines represent a distance of half a step height. The gray arrow represents the region where the wind turbine rotor might extend.

structure. The plot of TI ratio at  $x/h = -1.3$ , shown in Fig. 11, indicates that the flow structure is still quite compact.

By  $x/h = 0$ , the bursting has taken place. The speed-up of the streamwise flow through the vortex structure drops to 0.2, and the TI ratio increases accordingly.

While these observations are consistent with the vortex bursting described by the likes of Hall [22] and Gursul et al. [23], the bursting also needs to be considered in the context of the separation of the vortex from the crest of the geometry, which occurs in this, the shallowest  $A/\lambda$  case, and is evidenced by the weak recirculation back along the crest. The crest of the FFS beyond the stable node remains a source of vorticity. In the remaining cases, the stable node (or foci) occurs downstream of the trough.

Speed-up and TI ratio measurements for the  $A/\lambda = 0.5$  case are presented in Fig. 12 for planes at  $x/h = 1, 2, 4,$  and  $11$ , between heights of  $0.2h$  and  $2.4h$ . It is known that the primary vortex and the secondary vortices converge at the stable node, which is approximately  $0.5h$  downstream of the trough. The Cobra Probe measurements are taken downstream of the stable node, and the color plots in Fig. 12 demonstrate a strong retardation of the flow associated with the vortex cores. These downstream measurements are consistent with those from the shallower case—an expanded vortex core associated with low through-flow and high TI ratio.

While it is reasonable to expect that the bursting event would occur farther downstream as  $A/\lambda$  increases, the problem with

basing wind turbine siting on this assumption is the effect of wind directions not perpendicular to the cliff. A key observation from Ref. [10] was that one side of the sawtooth protrusion has a much higher effective  $A/\lambda$  resulting in a smaller vortex footprint and the other side has a much lower effective  $A/\lambda$ , resulting in a larger footprint. That is, the separation of the vortex from the crest of the sawtooth and the bursting of the vortex on the sawtooth protrusion, as observed in the  $A/\lambda = 0.325$  case, are inevitable for cases where  $A/\lambda > 0.325$ .

## Conclusions

Wind tunnel experiments using surface shear stress visualizations and surface pressure measurements have demonstrated the evolution of flow topology as a function of  $A/\lambda$  for wind flow over FFSs with sawtooth lateral variations. In addition, the vortex growth was mapped using the angle between the crest and the primary attachment line as a proxy. This was plotted against the Sawtooth Half Angle generated by the sawtooth lateral variation. In each case, the footprint of the vortex on the surface of the sawtooth protrusion occupied approximately half of the surface area.

Cobra Probe measurements demonstrated that vortex bursting is the mechanism that drives adverse flow conditions into the domain of wind turbine rotors. The burst vortex is associated with a distinct region of flow stagnation and, in the context of low TI conditions, an almost ten-fold increase in TI was observed. Above the sawtooth protrusion, as observed in the  $A/\lambda = 0.325$  case, the flow stagnation and the large shear associated with this are confined below a height of  $0.5h$ . Beyond the trough, the vertical extent of the vortex region increases from  $0.5h$  to beyond  $2h$  at  $10h$  downstream of the trough.

In the context of a similarly shaped real-world cliff, say, 100 m high, results from this study suggest that the vortex structures will persist well beyond 1 km downstream of the trough point. However, it is acknowledged that modeling was completed at very low levels of TI compared to actual ocean or land fetches on highly idealized models. Further work is required to understand the impact of increased levels of freestream TI and the extent to which the coherent structures would be broken down by increased levels of TI and the topology varied in the presence of nonidealized cliffs.

Over the sawtooth protrusion, the effects of the vortex structures are largely confined below 50 m above the surface. By the trough point, the increases in turbulence intensity and reduction in streamwise flow velocity are noticeable at heights between 50 m and 100 m; advancing downstream, the vertical extent of the flow deficit and increased TI increases to over 250 m above the surface with distance downstream. Given these observations and the tendency of the flow structures to align themselves with the freestream flow direction, approaches to siting where the wind turbines are sited in the far wake are unable to avoid the unfavorable flow conditions. By contrast, siting turbines on the sawtooth protrusions enables the rotor sweep to pass above the vortex structures and the associated shear layers. Applying the previous work of the current authors in characterizing flow over FFSs with different yaw angles, they recommended siting wind turbines  $0.5h$  downstream of the crest so as to avoid problems associated with inflow angles and wind veer [9]. Given the yawed FFS can be considered as a building block for the sawtooth FFS examined in this paper, applying the same rule of thumb is a reasonable approach for minimizing these effects. A schematic of the siting approach is presented in Fig. 13.

Future work on this topic by the current authors will model ruggedness as a sinusoidal lateral variation of the FFS in contrast to the sawtooth variation modeled here.

## Acknowledgment

Parts of this paper were first presented in the conference proceedings of the 17th Australasian Wind Engineering Society Workshop held in Wellington, New Zealand, in February 2015

entitled "Wind Turbine Siting on Rugged Cliffs". The authors wish to acknowledge the support of industry partner Entura.

## Funding Data

- The Australian Research Council's Linkage Project funding scheme, project number LP100100746.

## Nomenclature

$A$	= amplitude of sawtooth variation, m
$C_p$	= pressure coefficient
$h$	= height of cliff
$I_{uvw}$	= three-component turbulence intensity
$N$	= number of node points
$P$	= local pressure
$P_\infty$	= reference pressure
$Q_\infty$	= reference dynamic pressure
$S$	= number of saddle points; speed-up
$U_p$	= velocity, as measured by Pitot-static tube
$u, v, w$	= instantaneous components of velocity coincident with Cartesian coordinate system
$U, V, W$	= mean components of velocity coincident with Cartesian coordinate system
$v, w$	= Azimuthal and axial components of flow velocity, respectively
$x, y, z$	= length components oriented with Cartesian coordinate system

## Greek Symbols

$\alpha$	= power law shear exponent
$\delta$	= boundary layer thickness
$\varepsilon$	= angle through which the shear stress vector passes over the plane
$\lambda$	= wavelength of sinusoidal variation

## References

- [1] Bowen, A. J., and Lindley, D., 1977, "A Wind Tunnel Investigation of the Wind Speed and Turbulence Characteristics Close to the Ground Over Various Shaped Escarpments," *Boundary Layer Meteorol.* **12**(3), pp. 259–271.
- [2] Camussi, R., Felli, M., Pereira, F., Aloisio, G., and Di Marco, A., 2008, "Statistical Properties of Wall Pressure Fluctuations over a Forward Facing Step," *Phys. Fluids*, **20**(7), pp. 075113–075113-13.
- [3] Largeau, J. F., and Moriniere, V., 2007, "Wall Pressure Fluctuations and Topology in Separated Flows Over a Forward-Facing Step," *Exp. Fluids*, **42**(1), pp. 21–40.
- [4] Leclercq, D., Jacob, M., Louisot, A., and Talotte, C., 2001, "Forward-Backward Facing Step Pair: Aerodynamic Flow, Wall Pressure and Acoustic Characterisation," AIAA Paper No. AIAA-2001-2249.
- [5] Moss, W., and Baker, S., 1980, "Re-Circulating Flows Associated With Two-Dimensional Steps," *Aeronaut. J.*, **31**(3), pp. 151–172.
- [6] Ren, H., and Wu, Y.-T., 2011, "Turbulent Boundary Layers Over Smooth and Rough Forward-Facing Steps," *Phys. Fluids*, **23**(4), pp. 1–17.
- [7] Sherry, M., Lo Jacono, D., and Sheridan, J., 2010, "An Experimental Investigation of the Recirculation Zone Formed Downstream of a Forward Facing Step," *J. Wind Eng. Ind. Aerodyn.*, **98**(12), pp. 888–894.
- [8] Rowcroft, J., Burton, D., Blackburn, H. M., and Sheridan, J., 2014, "Surface Flow Visualisation Over Forward Facing Steps With Varying Yaw Angle," *J. Phys.: Conf. Ser.*, **555**(1), p. 012086.
- [9] Rowcroft, J., Burton, D., Blackburn, H. M., and Sheridan, J., 2015, "Siting Wind Turbines Near Cliffs—The Effect of Wind Direction," *Wind Energy*, **19**(8), pp. 1469–1484.
- [10] Cochard, S., Letchford, C. W., Earl, T. A., and Montlaur, A., 2012, "Formation of Tip-Vortices on Triangular Prismatic-Shaped Cliffs—Part 1: A Wind Tunnel Study," *J. Wind Eng. Ind. Aerodyn.*, **109**, pp. 9–20.
- [11] Montlaur, A., Cochard, S., and Fletcher, D. F., 2012, "Formation of Tip-Vortices on Triangular Prismatic-Shaped Cliffs—Part 2: A Computational Fluid Dynamics Study," *J. Wind Eng. Ind. Aerodyn.*, **109**, pp. 21–30.
- [12] Hoerner, S. F., and Borst, H. V., 1985, "Fluid-Dynamic Lift; Practical Information on Aerodynamic and Hydrodynamic Lift," Liselotte A. Hoerner, Bricktown, NJ.
- [13] Gad-el-Hak, M., and Blackwelder, R. F., 1985, "The Discrete Vortices From a Delta Wing," *AIAA J.*, **23**(6), pp. 961–962.
- [14] Lowson, M. V., Riley, A. J., and Swales, C., 1995, "Flow Structures Over Delta Wings," 33rd Aerospace Sciences Meeting, Reno, NV, Jan 9–12, p. 586
- [15] Gordnier, R., and Visbal, M. R., 1994, "Unsteady Vortex Structure Over a Delta Wing," *J. Aircr.*, **31**(1), pp. 243–248.

- [16] Gursul, I., 2005, "Review of Unsteady Vortex Flows Over Slender Delta Wings," *J. Aircr.*, **42**(2), pp. 299–319.
- [17] Wentz, W. H., and Kohlman, D. L., 1971, "Vortex Breakdown on Slender Sharp-Edged Wings," *J. Aircr.*, **8**(3), pp. 156–161.
- [18] Pearson, D. S., Goulart, P. J., and Ganapathisubramani, B., 2013, "Turbulent Separation Upstream of a Forward-Facing Step," *J. Fluid Mech.*, **724**, pp. 284–304.
- [19] Katz, J., 1999, "Wing/Vortex Interactions and Wing Rock," *Prog. Aerosp. Sci.*, **35**(7), pp. 727–750.
- [20] Rediniotis, O. K., Stapountzis, H., and Telionis, D. P., 1989, "Vortex Shedding Over Delta Wings," *AIAA J.*, **28**(5), pp. 944–946.
- [21] Rediniotis, O. K., Stapountzis, H., and Telionis, D. P., 1993, "Periodic Vortex Shedding Over Delta Wings," *AIAA J.*, **31**(9), pp. 1555–1562.
- [22] Hall, M. G., 1972, "Vortex Breakdown," *Annu. Rev. Fluid Mech.*, **4**(1), pp. 195–218.
- [23] Gursul, I., Gordnier, R., and Visbal, M., 2005, "Unsteady Aerodynamics of Nonslender Delta Wings," *Prog. Aerosp. Sci.*, **41**(7), pp. 515–557.
- [24] Goruney, T., and Rockwell, D., 2009, "Flow past a Delta Wing With a Sinusoidal Leading Edge: Near-Surface Topology and Flow Structure," *Exp. Fluids*, **47**(2), pp. 321–331.
- [25] Lange, J., Berg, J. M. J., Parvu, D., Kilpatrick, R., Costache, A., Chowdhury, J., Siddiqui, K., and Hangan, H., 2017, "For Wind Turbines in Complex Terrain, the Devil Is in the Detail," *Environ. Res. Lett.*, **12**(9), p. 094020.
- [26] LoTufo, J., 2017, "Full-Scale and Wind Tunnel Investigation of the Flow Field Over a Coastal Escarpment," *Master of Engineering Science*, University of Western Ontario, Canada, ON.
- [27] Rowcroft, J., 2015, "Investigation Into Wind Flow Over Complex Topography and Escarpments for Wind Turbine Siting," Ph.D., Monash University, Melbourne, Australia.
- [28] Mann, J., Angelou, N., Sjöholm, M., Mikkelsen, T., Hansen, K. H., Cavar, D., and Berg, J., 2012, "Laser Scanning of a Recirculation Zone on the Bolund Escarpment," *The Science of Making Torque From Wind*, IOP Publishing, Oldenburg, Germany.
- [29] Wai-Fah, C., and Lui, E. M., 2005, *Handbook of Structural Engineering*, 2nd ed., CRC Press, Boca Raton, FL.
- [30] Nieuwstadt, 1984, "The Turbulent Structure of the Stable, Nocturnal Boundary Layer," *American Meteorological Society*, *J. Atmos. Sci.*, **41**(14), pp. 2202–2216.
- [31] H., Wang, R. J., Barthelmie, S. C., Pryor, and H. G., Kim, 2014, "A New Turbulence Model for Offshore Wind Turbine Standards," *Wind Energy*, **17**(10), pp. 1587–1604.
- [32] Perry, A. E., and Chong, M. S., 1994, "Topology of Flow Patterns in Vortex Motions and Turbulence," *Appl. Sci. Res.*, **53**(3–4), pp. 357–374.
- [33] Hooper, J. D., and Musgrove, A. R., 1991, "Multi-Hole Pressure Probes for the Determination of the Total Velocity Vector in Turbulent Single-Phase Flow," Fourth International Symposium on Transport Phenomena in Heat and Mass Transfer Sydney, pp. 1364–1373.
- [34] Hooper, J. D., and Musgrove, A. R., 1997, "Reynolds Stress, Mean Velocity, and Dynamic Static Pressure Measurement by a Four-Hole Pressure Probe," *Exp. Therm. Fluid Sci.*, **15**(4), pp. 375–383.
- [35] Musgrove, A. R., and Hooper, J. D., 1993, "Pressure Probe Measurement of the Turbulent Stress Distribution in a Swirling Jet," Third World Conference on Experimental Heat Transfer, Fluid Mechanics and Thermodynamics, M. D. Kelleher, R. K. Shah, K. R. Sreenivasan, Y., Joshi, eds., pp. 172–179.
- [36] Crouch, T., Burton, D., Brown, N. A. T., Thompson, M. C., and Sheridan, J., 2014, "Flow Topology in the Wake of a Cyclist and Its Effect on Aerodynamic Drag," *J. Fluid Mech.*, **748**, pp. 5–35.
- [37] Bell, J. R., Burton, D., Thompson, M. C., Herbst, A., and Sheridan, J., 2014, "Wind Tunnel Analysis of the Slipstream and Wake of a High-Speed Train," *J. Wind Eng. Ind. Aerodyn.*, **134**, pp. 122–138.
- [38] Chen, J., Haynes, B. S., and Fletcher, D. F., 2000, "Cobra Probe Measurements of Mean Velocities, Reynolds Stresses and Higher-Order Velocity Correlations in Pipe Flow," *Exp. Therm. Fluid Sci.*, **21**(4), pp. 206–217.
- [39] Hunt, J. C. R., Abell, C. J., Peterka, J. A., and Woo, H., 1978, "Kinematical Studies of the Flows Around Free or Surface-Mounted Obstacles; Applying Topology to Flow Visualization," *J. Fluid Mech.*, **86**(1), pp. 179–200.
- [40] Werle, H., 1954, "Quelques Resultants Experimentaux Sur Les Ailes en Fleche, Aux Faibles Vitesses, Obtenus en Tunnel Hydrodynamique," *La Recherche Aeronautique*, **41**, pp. 15–21.
- [41] Castro, I. P., and Dianat, M., 1983, "Surface Flow Patterns on Rectangular Bodies in Thick Boundary Layers," *J. Wind Eng. Ind. Aerodyn.*, **11**(1–3), pp. 107–119.